Geophysical Journal International

Geophys. J. Int. (2013) **194,** 1559–1573
Advance Access publication 2013 May 11

doi: 10.1093/gji/ggt166

Ambient noise tomography across the Central Andes

Kevin M. Ward,[1] Ryan C. Porter,[2] George Zandt,[1] Susan L. Beck,[1] Lara S. Wagner,[3] Estela Minaya[4] and Hernando Tavera[5]

[1] *Department of Geosciences, The University of Arizona,* 1040 *E.* 4*th Street Tucson, AZ* 85721*, USA. E-mail: wardk@email.arizona.edu*
[2] *Department of Terrestrial Magnetism, Carnegie Institution of Washington,* 5241 *Broad Branch Road, NW, Washington, DC* 20015-1305*, USA*
[3] *Department of Geological Sciences, University of North Carolina at Chapel Hill,* 104 *South Rd., Mitchell Hall, CB* #3315*, Chapel Hill, NC* 27599-3315*, USA*
[4] *El Observatorio San Calixto, Calle Indaburo* 944*, Casilla* 12656*, La Paz, Bolivia*
[5] *Instituto Geofisico Del Peru, Calle Badajo No.* 169*, Urb. Mayorazgo IV Etapa, Lima, Peru*

Accepted 2013 April 22. Received 2013 April 8; in original form 2013 January 22

SUMMARY

The Central Andes of southern Peru, Bolivia, Argentina and Chile (between 12°S and 42°S) comprise the largest orogenic plateau in the world associated with abundant arc volcanism, the Central Andean Plateau, as well as multiple segments of flat-slab subduction making this part of the Earth a unique place to study various aspects of active plate tectonics. The goal of this continental-scale ambient noise tomography study is to incorporate broad-band seismic data from 20 seismic networks deployed incrementally in the Central Andes from 1994 May to 2012 August, to image the vertically polarized shear wave velocity (V_{sv}) structure of the South American Cordillera. Using dispersion measurements calculated from the cross-correlation of 330 broad-band seismic stations, we construct Rayleigh wave phase velocity maps in the period range of 8–40 s and invert these for the shear wave velocity (V_{sv}) structure of the Andean crust. We provide a dispersion misfit map as well as uncertainty envelopes for our V_{sv} model and observe striking first-order correlations with our shallow results (∼5 km) and the morphotectonic provinces as well as subtler geological features indicating our results are robust. Our results reveal for the first time the full extent of the mid-crustal Andean low-velocity zone that we tentatively interpret as the signature of a very large volume Neogene batholith. This study demonstrates the efficacy of integrating seismic data from numerous regional broad-band seismic networks to approximate the high-resolution coverage previously only available though larger networks such as the EarthScope USArray Transportable Array in the United States.

Key words: Interferometry; Surface waves and free oscillations; Seismic tomography; Crustal structure; South America.

1 INTRODUCTION

In recent years ambient noise tomography (ANT) has emerged as a powerful geophysical imaging tool capable of producing high-resolution images of structures in the crust and uppermost mantle. Traditional event-based surface and body-wave tomography studies are inherently limited by the geographic distribution of earthquakes and generally contain significantly less information about crustal structures than the ANT method can produce. In addition to providing detailed information about crustal structures, a distinct advantage of the ANT method is the ability to produce high-resolution dispersion maps on continental scales as exemplified by ANT studies across New Zealand, Europe, the United States, China, Australia and Tibet (Lin *et al.* 2007; Yang *et al.* 2007; Bensen *et al.* 2008; Zheng *et al.* 2008; Saygin & Kennett 2010; Yang *et al.* 2010). These continental-scale ANT studies have utilized extensive, and in the case of the EarthScope USArray Transportable Array (TA) in the United States (Meltzer *et al.* 1999), unprecedented broad-band seismic network coverage not available in all tectonically interesting parts of the world. The Central Andes in South America is one such area where the density of permanent broad-band seismic stations is inadequate and temporary seismic deployments are of insufficient duration and extent to produce the needed station density required for a traditional continental-scale ANT study of the Central Andes. Despite a nearly 20-yr history of publicly available broad-band seismic data collected in the Central Andes, few ANT studies have been published (Jay *et al.* 2012; Porter *et al.* 2012; Ma *et al.* 2013) and typically represent local to regional scales of coverage. As a result of an extensive data mining effort covering nearly 20 yr of data spanning seven distinct time periods, we construct a virtual seismic network suitable in extent to perform a high-resolution continental-scale ANT study of the Central Andes (Fig. 1). We present here, for the first time the vertically polarized shear wave velocity (V_{sv}) structure of the Central Andean crust derived from high-quality Rayleigh wave dispersion measurements across more than 1.5 × 10^6 km^2 of the South American Cordillera.

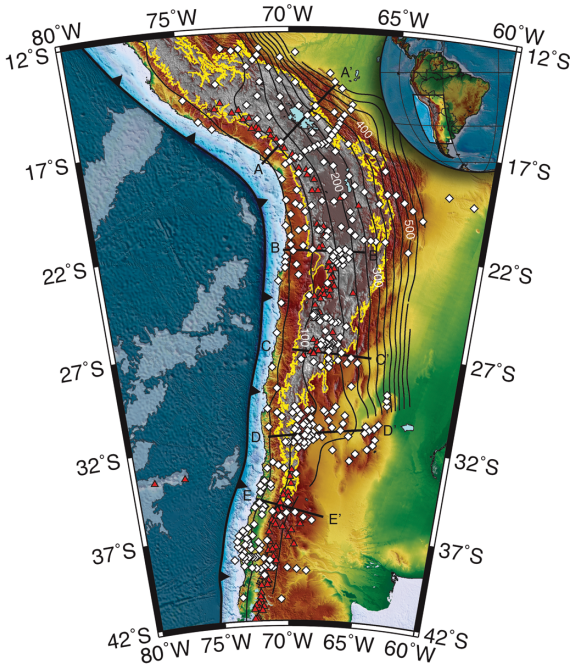

Figure 1. Map of our study area showing the bathymetry and topography, locations of seismic stations used in this study (white diamonds), locations of shear wave velocity cross-sections and Holocene volcanic activity (red triangles) from Siebert & Simkin (2002). The yellow line follows the 3-km-topography contour and defines the horizontal extent of Central Andean Plateau (CAP). The shaded white area offshore outlines the 4-km-bathymetry contour and defines the horizontal extent of anomalously thick oceanic crust. Slab contours in black (km) are from SLAB 1.0 (Hayes *et al.* 2012).

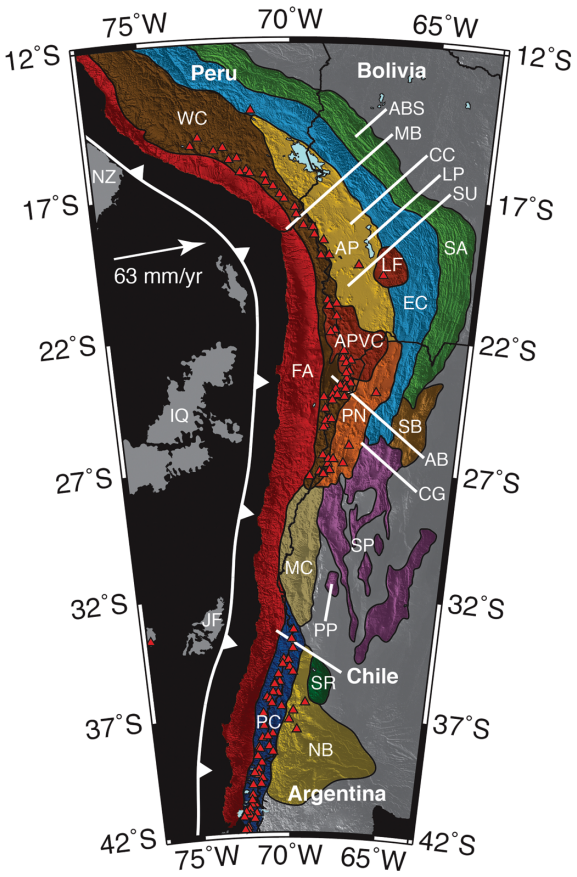

Figure 2. Map of major morphotectonic provinces (after Tassara 2005 and Turienzo *et al.* 2012) and geological features cited in text (after Cingolani & Varela 1999; Zandt *et al.* 2003; Placzek *et al.* 2006; Kay *et al.* 2010; Lamb 2011): the forearc (FA), the Western Cordillera (WC), the Altiplano (AP), the Eastern Cordillera (EC), the Subandes (SA), the Puna (PN), the Santa Barbara System (SB), the Main Cordillera, which includes from west to east, the Principal Cordillera, the Frontal Cordillera, and the Precordillera (MC), the Sierras Pampeanas (SP), the Principal Cordillera (PC), the Moquegua Basin (MB), the Alto-Beni Syncline (ABS), the Corque–Corocoro structure (CC), Lake Poopo (LP), the Salar de Uyuni (SU), the Altiplano-Puna Volcanic Complex (APVC), the Los Frailes Volcanic Complex (LF), the Atacama Basin (AB), Cerro Galan (CG), Sierra Pie de Palo (PP), the San Rafael basement block (SR), the Neuquén Basin (NB), the Nazca Ridge (NZ), the Iquique Ridge (IQ) and the Juan Fernandez Ridge (JF). Holocene volcanic activity (red triangles) from Siebert & Simkin (2002) and relative plate motion from Kendrick *et al.* (2003).

2 TECTONIC SETTING

The Central Andes of southern Peru, Bolivia, Argentina and Chile (between 12°S and 42°S) define the type example of an active Cordillera-type orogen where the tectonics are associated with subduction of the oceanic Nazca Plate under the continental South American Plate (Isacks 1988; Allmendinger *et al.* 1997; Lamb & Hoke 1997; Oncken *et al.* 2006; Tassara & Echaurren 2012). Numerical modelling suggests increased westward drift of the South American Plate has been an important mechanism driving tectonic shorting in the Cenozoic (Sobolev *et al.* 2006). Along-strike variations in the geometry of the east-dipping subducting Nazca slab (Fig. 1) have resulted in different styles of crustal deformation associated with segments of flat-slab subduction (Cahill & Isacks 1992). Characteristic volcanic cessation associated with the onset of the Peruvian (11 Ma) and Pampean (12 Ma) flat-slab subduction defines the northern and southern termination of the Central Volcanic Zone (CVZ) of the Central Andes (Ramos & Folguera 2009). Estimates of the current rate of convergence between the Nazca and South American plates are in the range of 58–80 mm yr^{-1} (Kendrick *et al.* 2003) with up to 15 mm yr^{-1} distributed over a broad zone of deformation that is the Central Andean Cordillera (Norabuena *et al.* 1998). Preferred shortening estimates are largest (>300 km) where the Andean orogen is widest (~20°S) with active deformation over 800 km inland from the trench (see summary in Gotberg *et al.* 2010). Both along-strike and across-strike variations in the style of tectonic deformation have segmented the Andes into distinct morphotectonic provinces, often with sharp boundaries (Kley *et al.* 1999). In the area of the Central Andean Plateau (CAP), the major morphotectonic provinces from west to east include: the forearc, the Western Cordillera, the Altiplano-Puna, the Eastern Cordillera and the Subandes (Fig. 2). South of the CAP where Pampean flat-slab subduction has driven deformation inboard of the Main Cordillera, active thick-skinned deformation in the Sierras Pampeanas extends nearly 800 km inland from the trench (Jordan *et al.* 1983).

The width of the modern forearc remains relatively constant throughout the study area (150–200 km) with a notable exception around 23°S where the active volcanic arc forms a westward concave bend that encompasses the Atacama Basin. Tectonic erosion since the late Neogene has led to the onset of subsidence and normal faulting in the offshore section of the forearc (Clift *et al.* 2003; von Huene & Ranero 2003). Normal faulting in the forearc continues onshore where the tectonic regime transitions from subsidence to uplift forming the Costal Cordillera (Allmendinger & Gonzalez 2010). The Northern Chilean Precordillera, the eastern most extent of the onshore forearc has experienced near-uniform trenchward tilt

during the Neogene and forms the western flank of the southern CAP (Isacks 1988; Victor *et al.* 2004; Jordan *et al.* 2010).

The Holocene age volcanic arc that defines the modern Western Cordillera is a collection of andesitic to dacitic stratovolcanoes that have erupted through older ignimbrite sheets. Variations in the mode of subduction since the mid-Eocene is thought to be responsible for a wider volcanic arc during the early Miocene that thermally weakened the lithosphere between 14°S and 24°S (Allmendinger *et al.* 1997; Ramos & Folguera 2009; Mamani *et al.* 2010). Previous seismological studies have imaged a consistently thick (∼70 km) Central Andean crust below the active volcanic arc and compositional variations in subduction-related igneous rocks suggest the crustal thickness has been increasing since the mid-Oligocene (Schmitz *et al.* 1999; Beck & Zandt 2002; Yuan *et al.* 2002; Mamani *et al.* 2010).

The Altiplano and Puna comprise the core of the CAP and are characterized by areas of high elevation with low (Altiplano) to moderate (Puna) relief. During the Cenozoic, the Altiplano has been the locus of sedimentation, with thick sequences of red-beds, evaporites and volcanics (Sobel *et al.* 2003; Strecker *et al.* 2007). The Corque–Corocoro structure, a fold and thrust zone that deforms thick sections of Eocene or Oligocene to Pliocene red-bed sequences occupies much of the northern Altiplano (Lamb 2011). Lake Poopo and the Salar de Uyuni are the remnants of a large palaeolake referred to as the Lake Tauca highstand that covered the entire southern Altiplano as recently as 14.1 ka (Placzek *et al.* 2006). Located at the transition between the Altiplano (average elevation 3700 m) and the Puna (average elevation 4200 m) is the Altiplano-Puna Volcanic Complex (APVC), a large silicic volcanic field with multiple young (∼12 to 1 Ma) ignimbrite eruptions (de Silva 1989; Kay *et al.* 2010; Salisbury *et al.* 2011). Underlying the APVC at a depth of 15–20 km is a thin (1–2 km) very low-velocity zone (∼1 km s^{-1} shear wave velocities) referred to as the Altiplano-Puna Magma Body (APMB; Chmielowski *et al.* 1999; Zandt *et al.* 2003).

The high topography that defines the eastern flank of the CAP and the Eastern Cordillera is composed of folded and faulted Palaeozoic rocks intruded by Triassic and Tertiary granitoid bodies (Benjamin *et al.* 1987; Gillis *et al.* 2006). In the north where the plutons outcrop along the western section of the Eastern Cordillera, elevations can exceed 6000 m and form the Cordillera Real. The eastern section of the Eastern Cordillera is predominantly the oldest stratigraphic section of the orogen with Ordovician age and locally older rocks outcropping. Significant upper-crustal shortening in the Eastern Cordillera ended before 10 Ma extending the active deformation front eastward into the Subandean Zone (Gubbels *et al.* 1993; Horton & DeCelles 1997; Echavarria *et al.* 2003). The Subandean Zone accommodates the transition from the high elevations of the CAP to the foreland plains through synclinal basins separated by thrust-faulted anticlines (McQuarrie *et al.* 2008). The Alto-Beni syncline, a piggyback basin that marks the western most extent of the Subandean Zone, has accommodated 6500–7000 m of Tertiary fill (Baby *et al.* 1995) and represents the transition in deformation style from thick-skinned (Eastern Cordillera) to the active thin-skinned deformation front (Subandean Zone).

Coeval with the initiation of Pampean (12 Ma) flat-slab subduction and subsequent eastward migration of magmatic activity south of the CAP, thermal weakening of the crust facilitated migration of the active deformation front east of the Preordillera and into the thick-skinned basement-cored block uplifts of the Sierras Pampeanas (Ramos *et al.* 2002). The Sierras Pampeanas are considered a modern deformation analogue to the basement-cored uplifts separated by sediment-filled basins observed in the Laramide orogeny of the North American Cordillera (Jordan & Allmendinger 1986). South of the Pampean flat-slab section (between 28°S and 33°S), the width of the orogen narrows along the San Rafael basement block and the modern deformation front is confined to the eastern extent of the Principal Cordillera (Fig. 2).

3 DATA AND METHODS

The fundamental basis for ANT is that the cross-correlation of ambient seismic noise as recorded by two contemporaneously operating seismometers can be used to extract surface wave empirical Green's functions (EGFs) for the path between the two stations (Sabra *et al.* 2005; Shapiro *et al.* 2005). While in principle both body waves (Roux *et al.* 2005; Poli *et al.* 2012) and surface waves (Shapiro *et al.* 2005; Moschetti *et al.* 2007; Yang *et al.* 2007) can be measured in this way, the main sources of coherent ambient noise are surface waves which dominates the amplitude of the Green's function between seismic stations making them easier to extract. The use of an automated frequency time analysis (FTAN) to measure the dispersion of group and phase velocities from inferred surface wave EGFs is well established in continental areas (Bensen *et al.* 2007; Moschetti *et al.* 2007; Lin *et al.* 2008). The spatial resolution of ANT is governed by the number, density and azimuthal distribution of good quality interstation dispersion measurements, which to first order, are a function of the number of seismic stations in the array, the geometry of the array and the length of the time window for which contemporaneous seismic data are available. For this reason, seismic arrays with close interstation spacing, large footprints and deployment durations of a year or longer are best suited for an ambient noise study (Bensen *et al.* 2007).

3.1 Data and initial processing

We recently deployed 50 broad-band seismic stations as part of the National Science Foundation (NSF) Continental Dynamics (CD) project: Central Andes Uplift and the Geodynamics of High Topography (CAUGHT) in the Central Andes of northern Bolivia and southern Peru. We augment the CAUGHT network with seismic data from 19 additional temporary and permanent deployments to construct an array ideally suited for an ambient noise study of the Central Andes (Fig. 1). Although the ambient noise method requires the cross-correlation of contemporaneously operating seismometers, we exploit the methods ability to incorporate interstation dispersion curves measured from previous deployments by supplementing our main array with data from six additional time periods. In total, we incorporate the vertical component from 330 broad-band seismic stations from 20 different international seismic networks (Table 1), deployed incrementally in the Central Andes from 1994 May to 2012 August, to image the vertically polarized shear wave velocity (V_{sv}) structure of the Central Andean crust. We follow the method outlined by Bensen *et al.* (2007) to obtain and quality control interstation surface wave dispersion measurements and briefly describe the data processing scheme used in this paper.

Initial quality control measures include visually inspecting the raw waveforms for instrument irregularities and non-seismic signals, which may pass subsequent filters and introduce spurious artefacts in the model results. Individual seismic station processing in the time domain includes cutting the waveform data into single-day segments, removing the mean, trend and instrument response, followed by applying a 5–150 s bandpass filter. Temporal normalization is done using a running-absolute-mean

Table 1. Seismic networks and number of seismic stations incorporated into this ANT study: Broadband Andean Joint Experiment/Seismic Exploration of Deep Andes (BANJO/SEDA; Beck *et al.* 1996), Bolivian Experiment (APVC; Chmielowski *et al.* 1999), Integrated Seismological Experiment in the Southern Andes (ISSA; Bohm *et al.* 2002), Receiver Function Central Andes (ReFuCA) Project (Heit *et al.* 2008), Chile Argentina Experiment (CHARGE; Alvarado *et al.* 2005), Sierras Pampeanas Experiment using a Multicomponent Broadband Array (SIEMBRA; Gans *et al.* 2011), Integrated Plate Boundary Observatory Chile (IPOC; Sodoudi *et al.* 2011), International Maule Aftershock Deployment (IMAD; Lange *et al.* 2012), The Puna Seismic Experiment (PUNA; Bianchi *et al.* 2012), Eastern Sierras Pampeanas (ESP; Richardson *et al.* 2012), Peru Subduction Experiment (PeruSE; Phillips *et al.* 2012).

Experiment Name	Network	No. of stations	Experiment
Global Seismograph Network (IRIS/USES)	IU	1	GSN
Global Telemetered Seismograph Network (GT)	GT	2	GT
Global Seismograph Network (GEOSCOPE)	G	1	GEOSCOPE
Global Seismograph Network (IRIS/IDA)	II	1	GSN
Integrated Seismological Experiment in the Southern Andes (ISSA)	SA	16	ISSA
Chile Argentina Experiment (CHARGE)	YC	23	CHARGE
Eastern Sierras Pampeanas (ESP)	XH	12	ESP
Maule Aftershock Deployment (UK)	3A	21	IMAD
Maule Earthquake (Chile) Aftershock Experiment	XS	37	IMAD
Sierras Pampeanas Experiment using a Multicomponent Broadband Array (SIEMBRA)	ZL	43	SIEMBRA
The Puna Seismic Experiment (PUNA)	X6	26	PUNA
Integrated Plate Boundary Observatory Chile (IPOC)	CX	20	IPOC
Investigating the Pluton Growth and Volcanism (PLUTONS)	XP	17	PLUTONS
Receiver Function Central Andes (ReFuCA) Project	RF	18	ReFuCA
Temp (GEOFON) Network	TE	5	GEOFON
Bolivian Experiment (APVC)	XH	7	APVC
Broadband Andean Joint Experiment / Seismic Exploration of Deep Andes (BANJO/SEDA)	XE	21	BANJO/SEDA
Peru Subduction Experiment (PeruSE)	TO	3	PeruSE
Peru Lithosphere and Slab Experiment (PULSE)	ZD	8	PULSE
Central Andes Uplift and the Geodynamics of High Topography (CAUGHT)	ZG	48	CAUGHT

normalization that acts to identify and remove the obscuring signals of earthquakes, instrument irregularities and non-stationary noise sources. The normalized time series are transformed into the frequency domain using a fast Fourier transform and spectrally whitened to produce a broader-band signal. We cross-correlate each possible single-day station pair segment, yielding over 3.5 million cross-correlations, transform them back into the time domain and stack unique station pairs to increase the signal-to-noise ratio (SNR). The causal and acausal components of the cross-correlated time function (Fig. S1) represent Rayleigh waves traveling in opposite directions between stations and are added to each other to reduce the effects of inhomogeneous source distribution. The resulting symmetric waveform component is an EGF from which a frequency–time analysis is performed to measure the phase velocities at 11 periods between 8 and 40 s. As we cross correlate only the vertical component of the three-component broad-band seismometer, our phase velocity results present Rayleigh waves which provide no information on the horizontally polarized shear wave velocity (V_{sh}) structure. The automation of calculating large numbers of interstation dispersion measurements allows for the introduction of spurious measurements into the data set and additional quality control measures must be applied. An initial attempt to remove obvious outliers discards dispersion measurements with phase velocities below 1.5 km s^{-1} and above 5.0 km s^{-1}. Individual phase velocities at periods associated with wavelengths longer than half of the interstation distance or with SNRs of less than 10 are removed from the dispersion measurements.

3.2 Phase velocity inversion

We use the remaining dispersion measurements to invert for phase velocity maps at 11 periods between 8 and 40 s using the method outlined by Barmin *et al.* (2001). As a final measure of quality control, dispersion measurements with residuals greater than 3 s are removed. Although the number of high-quality interstation dispersion measurements varies as a function of period (Table S1), the travel path density and coverage remains high across all 11 periods (Fig. S2). The relatively dense station spacing used in this study allows us to partition our study area into small $0.1^\circ \times 0.1^\circ$ geographic gridpoints and use less restrictive regularization parameters in the inversion. The penalty function used in the inversion is dependent on three user defined regularization parameters: α is a measure of the damping, β controls how data are smoothed in areas of varying path density and σ is the Gaussian smoothing width in kilometre. As suggested by Barmin *et al.* (2001), the selection of the best regularization parameters is somewhat arbitrary but can be improved upon by systematically varying the parameters and comparing the results with *a priori* information. We test the effects of varying the damping value, smoothing value, and smoothing length and conclude that the best regularization parameters for our study area are $\alpha = 200$, $\beta = 100$ and $\sigma = 50$ km. The merits of our preferred regularization parameters are presented briefly in the following section and we direct the reader to Barmin *et al.* (2001) for a detailed explanation of how the regularization parameters are developed. Inverting for phase velocity maps also yields a measure of spatial resolution at each gridpoint that is defined as the minimum separation distance at which two δ-like anomalies can be resolved (Barmin *et al.* 2001).

3.3 Sensitivity test for phase velocity inversion

We test the sensitivity of our phase velocity results by investigating the effects of systematically varying the regularization parameters and grid spacing used in the inversion. A comparison of phase velocity maps using $0.25^\circ \times 0.25^\circ$ with $0.1^\circ \times 0.1^\circ$ geographic grid spacing introduces minimal variation in the model results and we prefer the smooth appearance of the shear wave inversion results by using $0.1^\circ \times 0.1^\circ$ grid spacing. Varying the regularization parameters β and σ affects the amplitudes of anomalies on the edge of

our array with lower β and σ values allowing for larger amplitude ranges. We address the arbitrary nature of selecting the regularization parameters β and σ by favouring conservative values ($\beta = 100$ and $\sigma = 50$ km) and focusing our interpretations on areas with good resolution away from the peripheral of our model. The selection of the regularization parameter α (damping value) has the largest effect on our phase velocity results and warrants careful consideration.

We introduce a new metric that we call the 'roughness' in an attempt to quantify the best damping value to use for our study area. The roughness is defined as

$$\xi(\alpha, \lambda, \phi) = \left\{ \sum_{i=1}^{10} \left[c(\alpha, T_{i+1}, \lambda, \phi) - c(\alpha, T_i, \lambda, \phi) \right]^2 \right\}^{1/2}, \quad (1)$$

where ξ is the roughness, α is the damping value, λ is the latitude in degrees, ϕ is the longitude in degrees, c is the phase velocity in km s^{-1} and T is the period in seconds defined by the vector

$$T(i = 1, 2, 3, \ldots 11) = (8, 10, 12, 14, 16, 18, 20, 25, 30, 35, 40). \quad (2)$$

The roughness is a measure of the average rate of change in velocity between periods for a given 1-D phase velocity profile as a function of the damping value used in the inversion. As a perfectly resolved model would exhibit varying average rates of change between periods as a function of location due to the seismic heterogeneity of the Earth, we calculate the arithmetic mean of the roughness for each gridpoint in the model as a function of the damping value (α). The mean roughness has no inherent physical meaning, however, plotting the mean roughness ($\bar{\xi}$) against the damping value (α) provides a quantitative measure of assessing the effects the damping value has on the average roughness of the 1-D phase velocity profiles (Fig. 3a). The largest roughness values are observed for damping values below 150 and achieve stability somewhere between damping values of 150 and 250. Since the mean roughness value represents the mean of the entire model, we evaluate the distribution of the roughness as a function of each geographic gridpoint to ensure the mean roughness is representative of the entire model. The damping value of 200 produces a near-Gaussian, positivity-skewed distribution with the lowest discrepancy between the mean and mode of the distribution (Fig. 3b). For the aforestated reason and subsequent correlation with observable surface geology and morphotectonic provinces (*a priori* information), we select the damping value (α) of 200 as our preferred damping value.

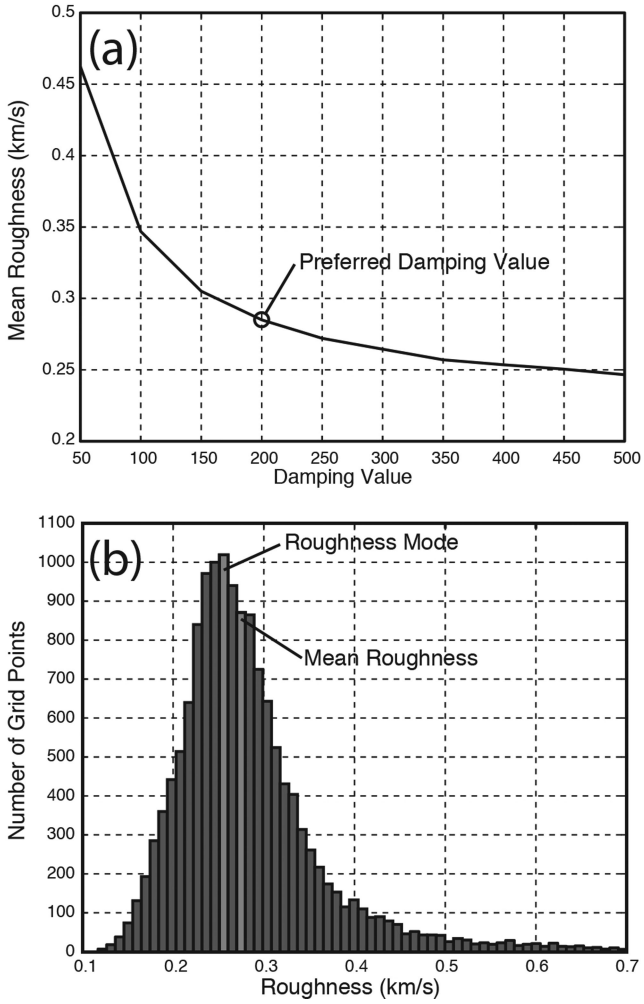

Figure 3. (a) Plot of mean roughness versus damping values used in the 2-D phase velocity inversion. (b) Distribution of roughness for each gridpoint in the model with mode and mean.

3.4 Shear velocity inversion

From the phase velocity maps at 8, 10, 12, 14, 16, 18, 20, 25, 30, 35 and 40 s, we construct phase velocity profiles at every gridpoint in our array. At each gridpoint where all 11 periods used to construct the phase velocity profiles have at least good resolution (<100 km), we iteratively invert for the 1-D shear wave velocity structure (Snoke & James 1997; Herrmann & Ammon 2004; Larson *et al.* 2006). Parametrizing the data for use in the shear wave inversion by the abovementioned way defines the horizontal extent of the shear wave inversion results and ensures that only phase velocity measurements with uniformly good resolution are used in the inversion. We use a linearized least-square inversion method that requires a 1-D shear wave velocity starting model and then iteratively inverts for the best 1-D shear wave velocity structure that minimizes the misfit between the calculated and observed 1-D phase velocity profile (Herrmann & Ammon 2004). Again, the selection of the damping value has a large effect on our shear wave velocity results and warrants additional consideration.

We calculate the arithmetic mean of the data misfit as a function of damping value and inversion iteration number and plot that against the arithmetic mean of the model perturbation norm, also a function of damping value and inversion iteration number (Fig. 4). Analysing the shear wave inversion in this fashion yields an independent measure of the relative effects of damping and the number of iterations on the mean data misfit. This is significant as the effects of damping and the number of iterations on the mean data misfit is intrinsically linked and often difficult to separate. After three iterations, we observe no significant reduction in the data misfit verses the model norm for all damping values and terminate the iterative inversion. Having determined the final number of iterations, we select the 0.5 damping value (dashed black line in Fig. 4) as it yields the lowest data misfit after three iterations. The measure of data misfit is again a mean measure of the entire model and we investigate the differences in misfit at individual gridpoints by plotting the period-averaged misfit for each geographic gridpoint in our study area (Fig. 5). Period averaged-dispersion misfit is defined as

$$\varepsilon(\lambda, \phi) = \frac{1}{n} \left\{ \sum_{i=1}^{n} \left[c_{\text{obs}}(T_i, \lambda, \phi) - c_{\text{pre}}(T_i, \lambda, \phi) \right]^2 \right\}^{1/2}, \quad (3)$$

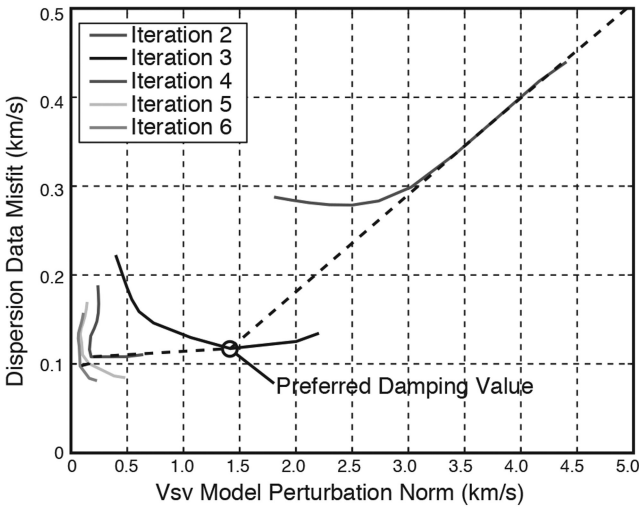

Figure 4. Plot of dispersion data misfit versus V_{sv} model perturbation norm as a function of damping value and iteration number used in the 3-D shear wave velocity inversion. Black dashed line shows the dispersion data misfit path of the 0.5 damping value after each iteration. Curves for each iteration connect the plotted values for each of 11 damping values (0.05, 0.1, 0.5, 1, 2, 3, 4, 5, 6, 7 and 8) evaluated in the shear wave inversion (Herrmann & Ammon 2004). Results from the first iteration are well off the plot and not shown.

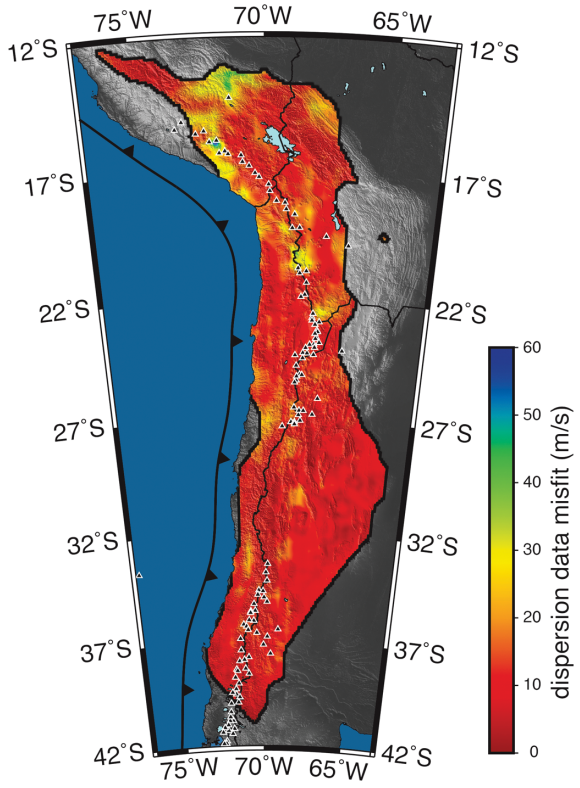

Figure 5. Period-averaged dispersion misfit map showing the difference from the 1-D dispersion curves and the dispersion curves calculated for each geographic gridpoint in the final 3-D shear wave velocity model.

where ε is the period-averaged dispersion misfit, n is the number of periods used, λ is the latitude in degrees, ϕ is the longitude in degrees, T is the period in seconds defined by the vector in eq. (2), c_{obs} is the observed phase velocity in km s^{-1} and c_{pre} is the phase velocity in km s^{-1} calculated from the shear wave model.

We observe comparable quality dispersion misfits as previous surface wave tomography studies (Yang *et al.* 2008) indicating our shear wave inversion parameters are appropriate for our study area. We find additional confidence for our preferred shear wave inversion parameters as evidenced by good first-order agreement between our shear wave velocity and phase velocity results, which in turn are in good agreement with observable surface geology and morphotectonic provinces.

3.5 Sensitivity test for shear velocity inversion

Inverting the phase velocity profiles for 1-D shear wave velocity profiles adds an additional complexity in quantifying the uncertainty of our results. We investigate the effects of varying the velocity structure and layer thicknesses for each location in our model by systematically inverting for the 1-D shear wave velocity profile using each possible permutation of two different layer thicknesses in the top 75 km of the starting model (1 and 5 km), three V_p/V_s ratios that are held constant (1.70, 1.75 and 1.80), three different Q values (50, 200 and 500) and four different constant velocity starting models (3.1, 3.6, 4.1 and 4.6 km s^{-1}). The minimum and maximum shear wave results for any given depth at each location define an envelope of uncertainty in our model results (Figs 6a–d). The uncertainty envelopes in the shallower depth slices (5 and 15 km) are generally less than 30 m s^{-1} with local zones of higher (>30 m s^{-1}) uncertainly in the forearc and most notably in the Peruvian forearc. Larger uncertainty envelopes (>60 m s^{-1}) in the deeper depth slices (35 and 50 km) correlate with areas of poorer dispersion misfit (Fig. 5) and are concentrated in areas with thinner crust. We use the depth at which the constant velocity-starting model dependent 1-D shear wave velocity results diverge as a proxy for the lower limit of our depth resolution (∼50 km across our study area).

Surface waves are dispersive meaning different periods are sensitive to different depths. In general, with surface waves the peak sensitivity depth and the thickness of sensitivity increases as the length of the period of the surface wave increases. It is this property of surface waves that makes them insensitive to sharp velocity contrasts such as the Moho. Previous work over limited regions of our study area interpreted large variations in the Moho depth both perpendicular to and along strike of the Andes (Beck & Zandt 2002; Yuan *et al.* 2002; Gans *et al.* 2011; Sodoudi *et al.* 2011; Tassara & Echaurren 2012), which make extrapolating a detailed contour map of the Moho for our entire study at the scale we are able to resolve problematic. Hence, we favour a constant velocity starting model and allow the iterative inversion technique to model vertical velocity variations. Ultimately, we present the shear wave velocity results obtained from using a starting model with a constant velocity of 4.6 km s^{-1}, a V_p/V_s ratio of 1.75, a Q value of 200 and a 325-km-thick model parametrized into 1-km-thick layers in the top 75 km of the model. We do not imply that we have 1 km vertical resolution in the top 75 km of our model but rather, we prefer the appearance of the smooth model and observe little difference in the final model results obtained from 5-km-thick layers. The selection of a 4.6 km s^{-1} constant velocity starting model, albeit counterintuitive for our depth resolution, introduces the least amount of artefacts in our shear wave velocity results (see supporting information for an expanded discussion on the selection of our constant velocity starting model). The relatively tight nesting of our shear wave results across all end-member input values and different morphotectonic provinces

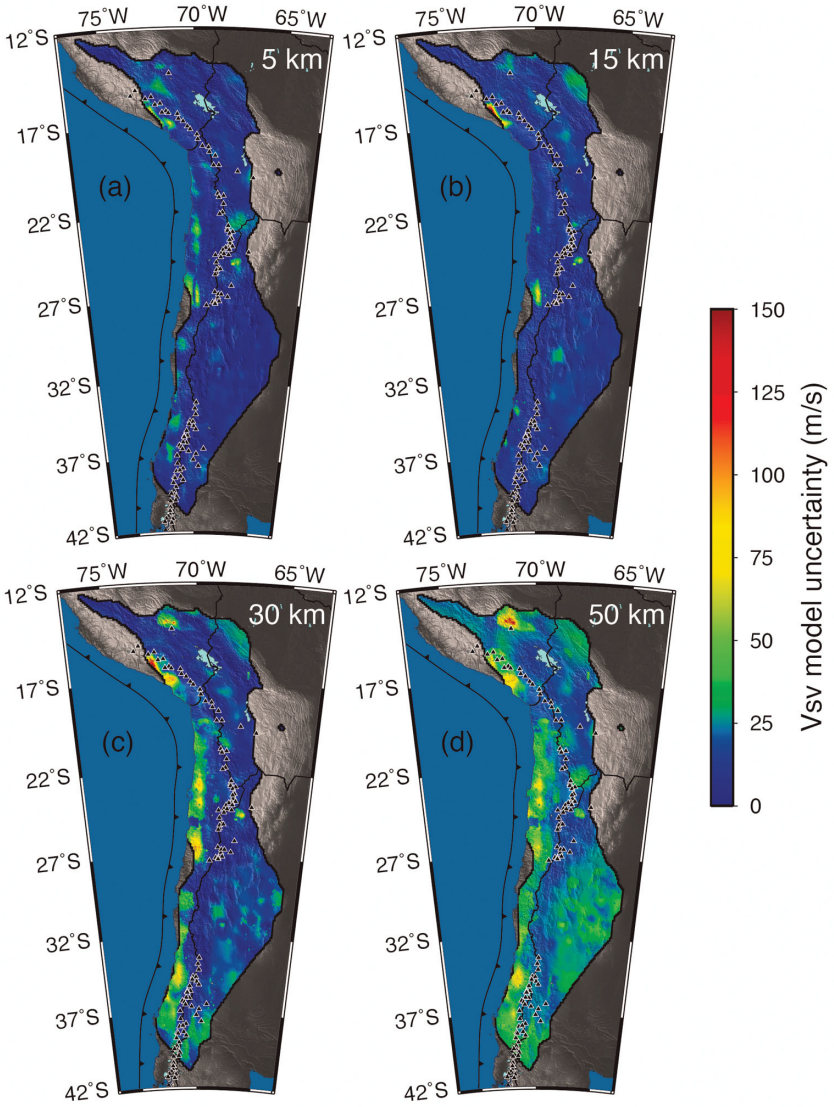

Figure 6. (a)–(d) Shear wave velocity model uncertainties at 5, 15, 30 and 50 km depth. Shear wave velocity model uncertainties are defined as the width of an envelope formed by systematically inverting for the 1-D shear wave velocity profile using each possible permutation of two different layer thicknesses in the top 75 km of the starting model (1 and 5 km), three V_p/V_s ratios that are held constant (1.70, 1.75 and 1.80), three different Q values (50, 200 and 500) and four different constant velocity starting models (3.1, 3.6, 4.1 and 4.6 km s^{-1}).

indicate our results are data driven and less dependent on *a priori* assumptions.

4 PHASE VELOCITY MAPS

The number of high-quality interstation dispersion curves peaks around 14–20 s and progressively decreases for periods longer than 20 s because of fundamental quality control requirements discussed in the previous section (SNR, interstation distance). Although the resolution of our phase velocity maps remains relatively constant between different periods (∼50 km), the horizontal extent of high-resolution coverage begins to decrease at 20 s and reaches the smallest extent at 40 s. By requiring every period used in the 1-D shear wave inversion to have at least good resolution (<100 km), we preserve the high-quality nature of our shear wave velocity model but effectively limit the horizontal scope of the model to the period with the smallest extent of high-resolution coverage (40 s). Additional information about the Andean crust is therefore available in phase velocity maps with periods shorter than 40 s and presented here (Figs 7a–c), not only as an intermediate step in the production of a 3-D shear wave velocity model, but as an additional geophysical imaging tool.

One of the lowest periods we can resolve across our array is 10 s (Fig. 7a), which reaches a peak sensitively around 6–10 km below the Earth's surface depending on the 1-D shear wave velocity structure. Comparing the phase velocity map at the 10-s period with known geological features and morphotectonic provinces is one way to appraise the robustness of our results both for 10 s and phase velocity measurements made for longer periods. In our phase velocity results at 10 s, we observe a striking first-order correlation with the morphotectonic provinces as well as more localized geological features such as the APVC and the uplifted Pie de Palo and San Rafael basement blocks. Aside from the location of the Los Frailes Volcanic Complex (LFVC), a large volume ignimbrite flare-up, the Eastern Cordillera is notably faster than the bounding basins of the Altiplano and the active thin-skinned fold-and-thrust belt of the Subandes with deep piggyback basins. Along the entire

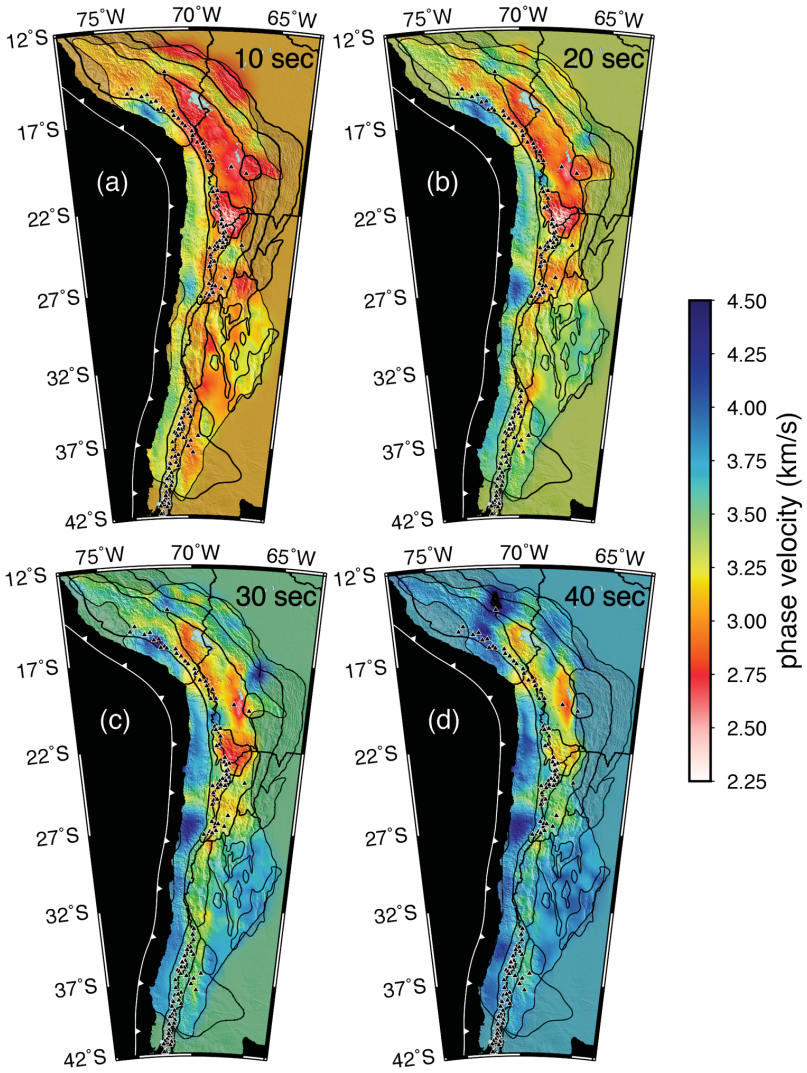

Figure 7. (a)–(d) Rayleigh wave phase velocity maps for 10, 20, 30 and 40 s with the same major morphotectonic provinces and Holocene volcanic activity (black triangles) shown in Fig. 2.

length of the forearc resolved in our study area (>2500 km), we observe faster velocities consistently bounded to the east by the slower velocities of the Western Cordillera, Main Cordilleran and Precordillera. The Sierras Pampeanas in Argentina provide the most stringent test of our phase velocity results due to the tightly nested alternating zones of low (basins) and high (uplifted basement blocks) velocities.

Phase velocity measurements at 20 s are the best constrained and also equal the largest range (2.5–4.3 km s^{-1}) of velocities for any one period (Fig. 7b). The most prominent feature at this depth slice is the anomalously low-velocity zone (~2.4 km s^{-1}) that corresponds to the location of the APMB imaged by previous seismic studies (Chmielowski *et al.* 1999; Zandt *et al.* 2003). Although smaller in volume, the LFVC located in the Eastern Cordillera at 19.5°S is similar in composition and timing to the APVC ignimbrite flare-up and we observe a comparable low-velocity zone below the LFVC that is persistent to at least 20 s. In the 30- and 40-s phase velocity results (Figs 7c and d), an extensive mid-crustal low-velocity body under the Altiplano and APVC is readily apparent against the considerably faster velocities observed in the areas of flat-slab subduction, where the crust is presumably colder and thinner.

5 DISCUSSION OF 3-D SHEAR VELOCITY MODEL

The final 3-D shear wave velocity (V_{sv}) model has been corrected for elevation and is presented in four depth slices (Figs 8a–d) and five cross-sections (Figs 9a–e). Two prominent first-order crustal-scale features observed in the ANT results are the thick high-velocity crust in the forearc, and the presence of an extensive mid-crustal low-velocity body under the western margin of the CAP. Both features have been recognized in earlier studies, but the larger-scale, uniform-resolution coverage of this ANT study provides a regional context for their interpretation. In this section, the ANT results are compared to previous seismic studies where there is overlap, and compared to other geophysical and geological studies to better constrain the interpretations of these features.

5.1 Forearc

At the upper limit of our resolution, a striking correlation is observed in our 5-km-depth slice with the morphotectonic provinces (Fig. 8a). The onshore forearc is characterized by fast velocities (~3.5 km s^{-1}) that follow the Coastal Cordillera, the mapped

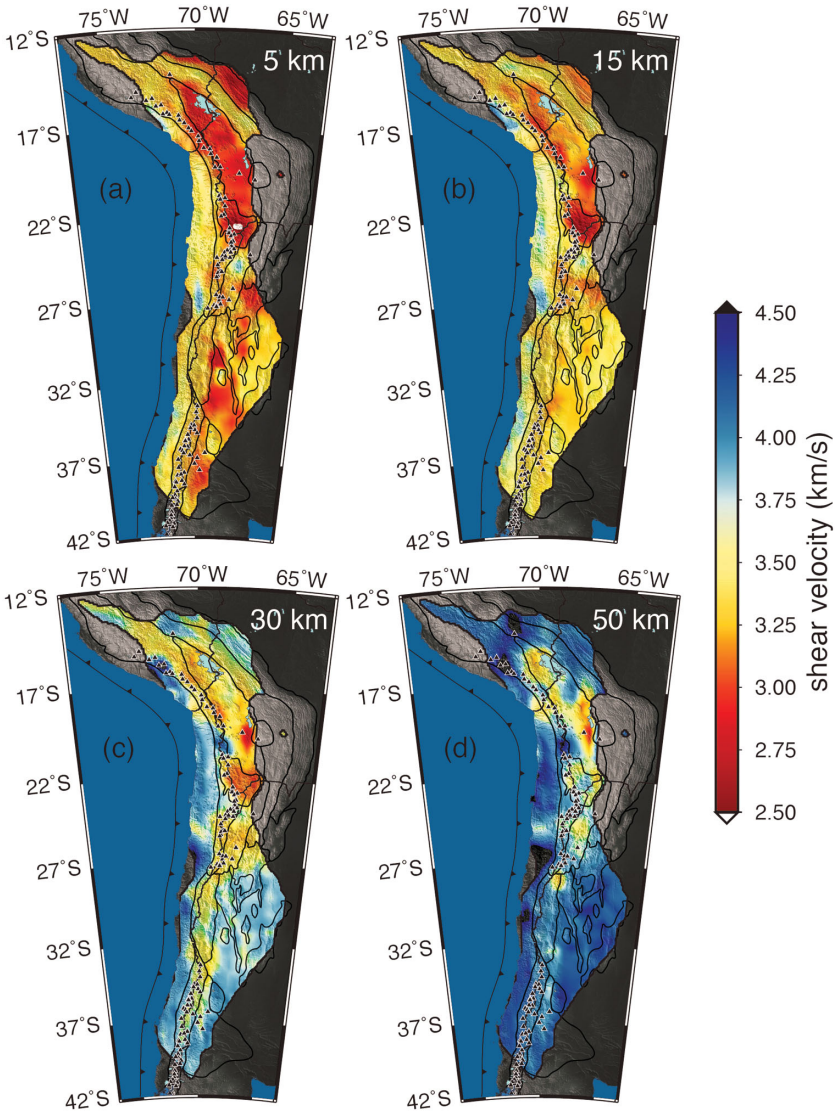

Figure 8. (a)–(d) Shear wave velocity (V_{sv}) model results at 5, 15, 30 and 50 km depth with the same major morphotectonic provinces and Holocene volcanic activity (black triangles) shown in Fig. 2.

location of a Palaeozoic batholith (Mamani *et al.* 2010). Near the coastal section of the axis of the Bolivian Orocline (∼18°S), the onshore section of the forearc is furthest from the trench and the Coastal Cordillera narrows and is no longer mapped onshore. Our results appear to capture this transition from high (∼3.5 km s^{-1}) velocities to low (∼3.0 km s^{-1}) and correlate well with the location of the southern Moquegua Basin (Rousse *et al.* 2005). At 15 km depth (Fig. 8b), the forearc is the fastest morphotectonic province and at 30 km (Fig. 8c) it is as fast as any other morphotectonic province with localized velocities of 4.5 km s^{-1}. At 50 km depth (Fig. 8d) the forearc is characterized by velocities that range from 3.75 to >4.5 km s^{-1}. Assuming that the 4.5 km s^{-1} value represents mantle material, this observation suggests a highly variable but generally large crustal thickness, given the relatively low elevations of the forearc. However, it is well known that forearc regions are often underlain by hydrated mantle that manifests itself with shear velocities that are low enough to appear crustal (Bostock *et al.* 2002; Hyndman & Peacock 2003; Manning 2004). Previous seismic studies in the Chilean forearc have interpreted the apparent large crustal thickness as an indicator of hydrated mantle (Schmitz *et al.* 1999) and our results are generally supportive of this idea.

The geological interpretation of the detailed seismic studies in the Chilean forearc is presented in Schmitz *et al.* (1999) and Giese *et al.* (1999), and only briefly summarized here. The prominent seismic discontinuity in the forearc at a depth of 35–45 km observed in both the active source and passive source models (where V_p reaches ∼7 km s^{-1}) is interpreted as the base of the Mesozoic lower crust, and its base as a 'blurred' continental palaeo-Moho. The depth interval between approximately 45 and 65 km is characterized by V_p between approximately 7 and 7.5 km s^{-1} and is interpreted as serpentinized upper mantle and the geophysical Moho at ∼65 km is suggested to represent the base of the stability field of serpentine and a transition to amphibole bearing peridotites. Our results image a forearc structure with crustal velocities (<4.5 km s^{-1}) extending to the lower limit of our depth resolution (Figs 9a and d) and is consistent with the presence of unusually thick crust, at least in a geophysical sense, in the absence of significant tectonic shortening (Giese *et al.* 1999). Our results also show that this thick geophysical crust extends the length of the forearc in the

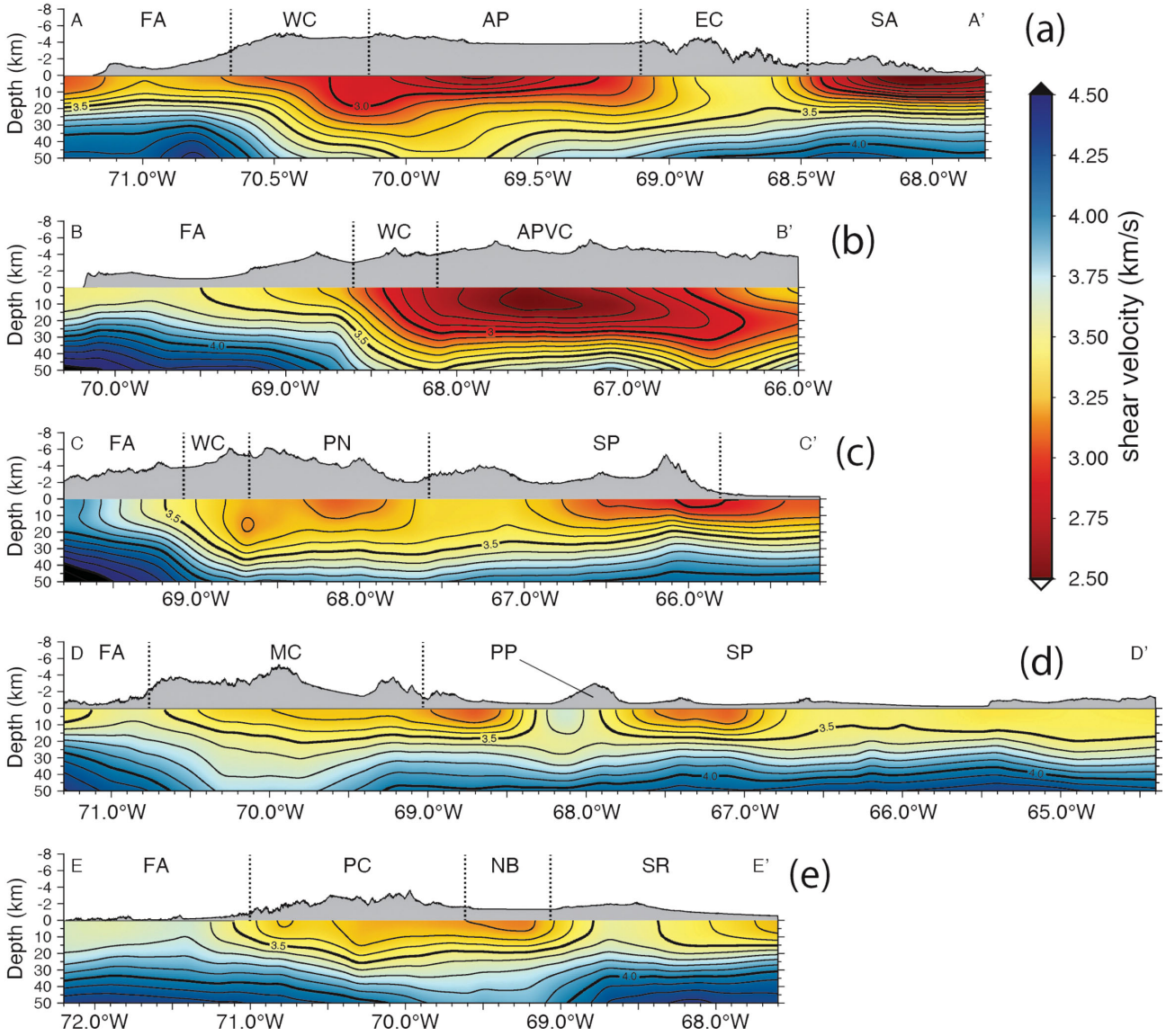

Figure 9. (a)–(e) Shear wave velocity model cross-sections illustrating the difference in the velocity structure of the Central Andes. Cross-section results are presented with no vertical exaggeration (1:1) and the locations are shown in Fig. 1 and abbreviations are defined in Fig. 2.

study area, from 15°S to 38°S with one possible exception near 27°S.

5.2 Western Cordillera

The WC is characterized by low velocities (2.75–3.25 km s^{-1}) in areas associated with Holocene volcanic activity transitioning into higher velocities (>3.0 km s^{-1}) in both the northern and southern margins of the CVZ that more closely resemble forearc velocities in the 5-km-depth slice (Fig. 8a). At 15 km depth (Fig. 8b), an almost continuous along strike low velocity body (<3.25 km s^{-1}) underlies the Western Cordillera with two notable exceptions at 20°S associated with the 'Pica Volcanic Gap' and at 24°S associated with the Central Andean Gravity High (Gotze & Krause 2002). This low velocity body appears to terminate near the southern limit of the CVZ around 28°S. Despite this complex relationship between the Western Cordillera morphotectonic province and the low velocity body, the active arc as marked by Holocene volcanoes is consistently located along the western edge of the body, until it terminates near 28°S. By 30 km depth (Fig. 8c) the Western Cordillera is no longer distinguishable by a distinctive velocity, but rather appears as a gradient zone between the higher velocities in the forearc and the lower velocities in the interior of the Altiplano-Puna.

5.3 Altiplano-Puna

The other major result from this ANT study is the observation of a major mid-crustal low-velocity body along the western margin of the Andean Plateau. Although most of the Andean Plateau velocities at 5 km depth (Fig. 8a) are below 3.0 km s^{-1}, the Altiplano-Puna is distinctly different from the rest of the Plateau with large sections of the Altiplano-Puna below 2.75 km s^{-1} and locally below 2.5 km s^{-1}. It has been known for some time that the CAP is supported by a thick, low average velocity crust (e.g. Beck & Zandt 2002) with a pervasive mid-crustal low-velocity layer, often called the Andean low-velocity zone (ALVZ; Yuan *et al.* 2000). Our results image a comparable low-velocity zone in the crust underneath the CAP that is considerably slower than the crust below the Pampean flat-slab

segment of the Central Andes. This velocity contrast is especially apparent in the cross-sections where the 3.5 km s^{-1} velocity contour under the CAP is deeper than 30 km and locally extends deeper than 50 km (Fig. 9a) whereas the 3.5 km s^{-1} velocity contour is shallower than 20 km below the Pampean flat-slab segment (Fig. 9d). The low average velocity reflects a predominantly felsic composition (Lucassen *et al.* 2001; Beck & Zandt 2002) and has been interpreted as a zone of crustal flow (Husson & Sempere 2003). An alternative interpretation for this observed low-velocity zone is magmatic in nature. At 15 km depth (Fig. 8b), the low velocity body (<3.25 km s^{-1}) that underlies much of the Western Cordillera extends eastward under the Altiplano-Puna and correlates with location of large Neogene ignimbrite eruptive centres (APVC, LFVZ, Cerro Galan) and negative isostatic residual gravity anomalies. Using the hypothesis that voluminous ignimbrites are the surface expression of batholith formation at depth, de Silva & Gosnold (2007) incorporate geochemical, ignimbrite eruptive histories, gravity data and seismic data to elucidate the linkage between the spatiotemporal development of ignimbrite flare-ups and batholith formation at depth. Their analysis suggests a thermally induced positive feedback magmatic system that promotes the accumulation of dacite magma bodies that evolves with time requiring the presence of a large batholith of intermediate to felsic composition beneath the APVC. If this linkage is correct, our results suggest the presence of a much larger batholith that underlies most of the southern Altiplano and northern Puna as well as the western side of the northern Altiplano. A detailed discussion of the provenance of the ALVZ is beyond the scope of this study, however, we interpret the 3.25 km s^{-1} contour at 15 km depth to generally outline the extent of a Neogene batholith with isolated pockets of partial melt and will develop this interpretation as the focus of subsequent papers.

5.4 APVC

The APVC is a late Cenozoic large-volume silicic volcanic centre located at the transition between the Altiplano and the high standing Puna province (de Silva 1989). The APVC and the crustal body of partial melt that supplies it (APMB) provide an additional test on the ability of our results to resolve crustal structures. The APVC of the Central Andes is one of the best-studied large silicic volcanic fields associated with an active subduction margin. As a result, multiple geophysical techniques have imaged a low velocity, high conductivity crustal 'magma body' centered on a depth of 15 km (Chmielowski *et al.* 1999; Brasse *et al.* 2002; Zandt *et al.* 2003; Pritchard & Simons 2004). Our results at the 15-km-depth slice (Fig. 8b) show a regionally extensive low-velocity body (<2.75 km s^{-1}) in the area of the APMB. Thus, our results at 15 km depth with $V_{sv} < 2.75$ km s^{-1} most likely represent a magma 'mush' zone with 15–20 per cent partial melt (Schilling & Partzsch 2001; Schilling *et al.* 2006). Magnetotelluric results from further north (∼18°S) do not resolve a mid-crustal high conductivity zone (Schilling *et al.* 2006; Brasse & Eydam 2008), which is consistent with our results.

5.5 Eastern Cordillera

The portion of the Eastern Cordillera where we have coverage is perhaps one of the best-resolved regions in the 5-km-depth slice (Fig. 8a). Flanked to the northeast by the thin-skinned fold-and-thrust belt of the Subandes with thick piggyback basins and to the southwest by the Altiplano basin, the basement-involved fold-and-thrust style of the Eastern Cordillera has formed a very distinctive shallow subsurface velocity structure. The low velocities (<3.0 km s^{-1}) of the Altiplano and Subandean basins stand in sharp contrast to the much higher velocities (>3.25 km s^{-1}) of the Eastern Cordillera where basement rocks outcrop or are located near the surface. This velocity contrast between the Eastern Cordillera and surrounding crust (Altiplano and Subandes) is persistent to depths of 15–20 km (Fig. 9a) and similar in extent to the Pie de Palo basement uplift in the Sierras Pampeanas (Fig. 9d). A few additional pockets of even higher velocity (>3.5 km s^{-1}) are distributed along the Cordillera Real segment of the Eastern Cordillera and correlate with the location of Triassic and Tertiary granitoid plutons (Benjamin *et al.* 1987; Gillis *et al.* 2006). In the 30 km depth slice (Fig. 8c), the distinction between the Subandes and the Eastern Cordillera is not as apparent as in the shallower results but the Eastern Cordillera maintains a generally higher velocity that defines the eastern limit of the Altiplano and the western edge of the Subandes.

5.6 Subandes

The Subandean zone accommodates the transition from the high topography of the CAP to the lowland elevation of the foreland basin through a series of active thin-skinned fold-and-thrust type structures. We have less coverage over this section of the Andes but where we can resolve the velocity structure, we observe low velocities (<2.75 km s^{-1}) at the 5-km-depth slice in the Subandes (Fig. 8a). The lowest velocities correlate with the Alto-Beni Basin, a large piggyback basin (Baby *et al.* 1995) that marks the westernmost extent of the Subandes (Fig. 9a). Shear wave velocities within the Subandes are mostly slower than in the Eastern Cordillera at 15 km (Fig. 8b) but by 30 km (Fig. 8c) the Subandes are faster than the Eastern Cordillera. At 50 km depth (Fig. 8d), the Subandean zone is as fast as the forearc likely reflecting the transition to a thinner crust in the foreland.

5.7 Sierras Pampeanas

The Sierras Pampeanas are the subject of detailed surface wave (both ambient noise and earthquake sourced surface wave tomography) and receiver function study (Gans *et al.* 2011; Porter *et al.* 2012) and for that reason we limit our discussion in this area. Our results incorporate data from more stations than previous studies and therefore resolve a larger portion of the crust both to the north and south of the Pampean flat-slab segment. As our focus in this study is imaging broader crustal-scale structures, a brief description and comparison with previous work is appropriate in the context of a continental-scale study. Our shear wave velocity results in the 5-km-depth slice (Fig. 8a) resolve the complex structure of the Sierras Pampeanas tightly nested alternating zones of low (basins) and high (basement-cored blocks) velocities. South of the location of Cerro Galan, a large volume ignimbrite centre, the basement-cored uplifts of the Sierras Pampeanas are notably faster than the sounding basins.

A prominent feature imaged in both this study and previous studies (Porter *et al.* 2012) is the westernmost Sierra Pie de Palo basement uplift where similar velocities (>3.25 km s^{-1}) are observed in the basement-involved uplifts of the Eastern Cordillera (Figs 9a and d). Sediment filled basins where our results image low velocities similar to the Alitplano and Alto-Beni basins bound the Sierra Pie de Palo basement uplift to the north and south.

By the 30-km-depth slice (Fig. 8c), the alternating zones of low (basins) and high (basement-cored blocks) velocities are no longer observed in the Sierras Pampeanas and the region is seismically faster than the Puna and Main Cordillera likely indicating the transition from the thicker crust (∼70 km) of the CAP to the thinner (<50 km) crust of the region. Previous studies have imaged a thick (>50 km) crust below sections of the Main Cordillera (Gans *et al.* 2011) and our results are generally supportive of this interpretation. At the 50-km-depth slice (Fig. 8d), the Main Cordillera consists of crustal velocities (<4.0 km s^{-1}) bounded to the west and east by the faster velocities (>4.0 km s^{-1}) of the forearc and Sierras Pampeanas.

5.8 Southern Andes

Our coverage south of the Pampean flat-slab segment is limited, imaging only the northernmost extent of the Southern Andes. A prominent feature observed in our results in the 5- and 15-km-depth slices is the San Rafael Block (Figs 8a and b), which exposes Mesoproterozoic age basement rocks surrounded by Cenozoic sediments and volcanics (Cingolani & Varela 1999). The San Rafael Block is bounded to the north by basins of the Sierras Pampeanas and to the west and south by the Neuquén Basin where the velocities are analogous to the velocities (<3.0 km s^{-1}) observed in the Altiplano and the Alto-Beni basins. Holocene volcanic-arc activity in the Principal Cordillera and back-arc volcanic activity in the westernmost section of the Neuquén Basin (Payenia Volcanic Complex) correlates with lower velocity zones in our 30-km-depth slice (Fig. 8c). At 50 km (Fig. 8d), the forearc is slightly faster than the crust below the Principal Cordillera and Neuquén Basin and the lower velocities of the Principal Cordillera are only slightly distinguishable form the crust below the Neuquén Basin.

6 CONCLUSIONS

We calculated the vertically polarized shear wave velocity (V_{sv}) structure of the Central Andean crust using Rayleigh wave phase velocities determined from the cross-correlation of ambient seismic noise. Striking first-order correlations with our shallow results (10 s and 5 km) and the morphotectonic provinces as well as subtler geological features indicate our results are robust and demonstrate the efficacy of integrating data from 20 different international seismic networks spanning seven distinct time periods. We provide dispersion misfit and V_{sv} model uncertainty maps and observe comparable values seen in previous studies (Yang *et al.* 2008) indicating that our results are capable of providing constraints on the structure of the crust to a depth of about 50 km. The focus of this paper has been to present the results of integrating numerous data sets into one single continuous 3-D shear wave velocity model of the South American Cordillera and we have limited our tectonic interpretation to substantiate our contention that this approach is appropriate for a continental-scale ANT study. Our results reveal for the first time the full extent of the mid-crustal ALVZ that we tentatively interpret as the signature of a very large volume Neogene batholith. This approach provides a unique opportunity to investigate the crustal-scale structures of an active orogenic belt on a scale of detail previously unavailable in smaller regional studies and we expect future work that incorporates our results with other geophysical and geological methods to address several fundamental tectonic problems related the nature of orogenic crust in oceanic-continental subduction settings.

ACKNOWLEDGEMENTS

Thanks to C. Berk Biryol for his help with this research. This work is supported by National Science Foundation award EAR-0739001, EAR-0907880, EAR-0943991, EAR-0909254 and EAR-1045597. Additional support was provided by ExxonMobil. The instruments used in the CAUGHT, PULSE, IMAD and SIEMBRA field programs were provided by the PASSCAL facility of the Incorporated Research Institutions for Seismology (IRIS) through the PASSCAL Instrument Centre at New Mexico Tech. Data collected during the CAUGHT and PULSE experiments will be available through the IRIS Data Management Centre. The facilities of the IRIS Consortium are supported by the NSF under Cooperative Agreement EAR-0552316 and by the Department of Energy National Nuclear Security Administration. We acknowledge the GEOFON Program of GFZ Potsdam as an additional source of waveform data. We further acknowledge all of those who helped to deploy, maintain and service the seismic stations from the 20 different international networks. Finally, we thank all the PIs from the PULSE, PLUTONS, Eastern Sierras Pampeanas and PeruSE experiments for sharing some of their restricted data prior to their release date. We also thank the Instituto Geofisico del Peru and the San Calixto Observatory in Bolivia for their help and logistical support. Chevron-Texaco, Conoco-Phillips and ExxonMobil provided additional support to Kevin M. Ward.

REFERENCES

Allmendinger, R.W. & Gonzalez, G., 2010. Invited review paper: Neogene to Quaternary tectonics of the coastal Cordillera, northern Chile, *Tectonophysics,* **495,** 93–110.

Allmendinger, R.W., Jordan, T.E., Kay, S.M. & Isacks, B.L., 1997. The evolution of the Altiplano-Puna plateau of the Central Andes, *Annu. Rev. Earth planet. Sci.,* **25,** 139–174.

Alvarado, P., Beck, S., Zandt, G., Araujo, M. & Triep, E., 2005. Crustal deformation in the south-central Andes backarc terranes as viewed from regional broad-band seismic waveform modelling, *Geophys. J. Int.,* **163,** 580–598.

Baby, P., Moretti, I., Guillier, B., Limachi, R., Mendez, E., Oller, J. & Specht, M., 1995. Petroleum system of the northern and central Bolivian sub-Andean zone, in *Petroleum Basins of South America,* pp. 445–458, eds Tankard, A.J., Suarez, R., Welsink, S. & Welsink, H.J., APPG Memoir 62.

Barmin, M.P., Ritzwoller, M.H. & Levshin, A.L., 2001. A fast and reliable method for surface wave tomography, *Pure appl. Geophys.,* **158,** 1351–1375.

Beck, S.L. & Zandt, G., 2002. The nature of orogenic crust in the central Andes, *J. geophys. Res.-Solid Earth,* **107,** 2230–2247.

Beck, S.L., Zandt, G., Myers, S.C., Wallace, T.C., Silver, P.G. & Drake, L., 1996. Crustal-thickness variations in the central Andes, *Geology,* **24,** 407–410.

Benjamin, M.T., Johnson, N.M. & Naeser, C.W., 1987. Recent rapid uplift in the Bolivian Andes—evidence from Fission-Track Dating, *Geology,* **15,** 680–683.

Bensen, G.D., Ritzwoller, M.H., Barmin, M.P., Levshin, A.L., Lin, F., Moschetti, M.P., Shapiro, N.M. & Yang, Y., 2007. Processing seismic ambient noise data to obtain reliable broad-band surface wave dispersion measurements, *Geophys. J. Int.,* **169,** 1239–1260.

Bensen, G.D., Ritzwoller, M.H. & Shapiro, N.M., 2008. Broadband ambient noise surface wave tomography across the United States, *J geophys. Res.-Solid Earth,* **113,** B05306.

Bianchi, M. *et al.*, 2012. Teleseismic tomography of the southern Puna plateau in Argentina and adjacent regions, *Tectonophysics,* **586,** 65–83.

Bohm, M., Luth, S., Echtler, H., Asch, G., Bataille, K., Bruhn, C., Rietbrock, A. & Wigger, P., 2002. The Southern Andes between 36 degrees and

40 degrees S latitude: seismicity and average seismic velocities, *Tectonophysics,* **356,** 275–289.

Bostock, M.G., Hyndman, R.D., Rondenay, S. & Peacock, S.M., 2002. An inverted continental Moho and serpentinization of the forearc mantle, *Nature,* **417,** 536–538.

Brasse, H. & Eydam, D., 2008. Electrical conductivity beneath the Bolivian Orocline and its relation to subduction processes at the South American continental margin, *J. geophys. Res.-Solid Earth,* **113,** B07109.

Brasse, H., Lezaeta, P., Rath, V., Schwalenberg, K., Soyer, W. & Haak, V., 2002. The Bolivian Altiplano conductivity anomaly, *J. geophys. Res.-Solid Earth,* **107**, doi:10.1029/2001JB000391.

Cahill, T. & Isacks, B.L., 1992. Seismicity and shape of the subducted Nazca Plate, *J. geophys. Res.-Solid Earth,* **97,** 17 503–17 529.

Chmielowski, J., Zandt, G. & Haberland, C., 1999. The Central Andean Altiplano-Puna Magma body, *Geophys. Res. Lett.,* **26,** 783–786.

Cingolani, C. & Varela, R., 1999. The San Rafael Block, Mendoza (Argentina): Rb-Sr isotopic age of basement rocks, in *Proceedings of the 2nd South. Am. Symp. Isotope Geol.,* Villa Carlos Paz, Argentina, pp. 23–26.

Clift, P.D., Pecher, I., Kukowski, N. & Hampel, A., 2003. Tectonic erosion of the Peruvian forearc, Lima Basin, by subduction and Nazca Ridge collision, *Tectonics,* **22,** 1023, doi:10.1029/2002TC001386.

de Silva, S.L. & Gosnold, W.D., 2007. Episodic construction of batholiths: insights from the spatiotemporal development of an ignimbrite flare-up, *J. Volc. Geotherm. Res.,* **167,** 320–335.

de Silva, S.L., 1989. Altiplano-Puna volcanic complex of the central Andes, *Geology,* **17,** 1102–1106.

Echavarria, L., Hernandez, R., Allmendinger, R. & Reynolds, J., 2003. Subandean thrust and fold belt of northwestem Argentina: geometry and timing of the Andean evolution, *AAPG Bull.,* **87,** 965–985.

Gans, C.R., Beck, S.L., Zandt, G., Gilbert, H., Alvarado, P., Anderson, M. & Linkimer, L., 2011. Continental and oceanic crustal structure of the Pampean flat slab region, western Argentina, using receiver function analysis: new high-resolution results, *Geophys. J. Int.,* **186,** 45–58.

Giese, P., Scheuber, E., Schilling, F., Schmitz, M. & Wigger, P., 1999. Crustal thickening processes in the Central Andes and the different natures of the Moho-discontinuity, *J. South Am. Earth Sci.,* **12,** 201–220.

Gillis, R.J., Horton, B.K. & Grove, M., 2006. Thermochronology, geochronology, and upper crustal structure of the Cordillera Real: implications for Cenozoic exhumation of the Central Andean Plateau, *Tectonics,* **25,** TC6007, doi:10.1029/2005TC001887.

Gotberg, N., McQuarrie, N. & Caillaux, V.C., 2010. Comparison of crustal thickening budget and shortening estimates in southern Peru (12–14 degrees S): implications for mass balance and rotations in the "Bolivian orocline," *Geol. Soc. Am. Bull.,* **122,** 727–742.

Gotze, H.J. & Krause, S., 2002. The Central Andean Gravity High, a relic of an old subduction complex? *J. South Am. Earth Sci.,* **14,** 799–811.

Gubbels, T.L., Isacks, B.L. & Farrar, E., 1993. High-level surfaces, plateau uplift, and foreland development, Bolivian Central Andes, *Geology,* **21,** 695–698.

Hayes, G.P., Wald, D.J. & Johnson, R.L., 2012. Slab1.0: a three-dimensional model of global subduction zone geometries, *J. geophys. Res.-Sol Ea,* **117,** doi:10.1029/2011JB008524.

Heit, B., Koulakov, I., Asch, G., Yuan, X., Kind, R., Alcocer-Rodriguez, I., Tawackoli, S. & Wilke, H., 2008. More constraints to determine the seismic structure beneath the Central Andes at 21 degrees S using teleseismic tomography analysis, *J. South Am. Earth Sci.,* **25,** 22–36.

Herrmann, R.B. & Ammon, C., 2004. *Computer Programs in Seismology, Version 3.30,* Department of Earth and Atmospheric Sciences, Saint Louis University, Missouri.

Horton, B.K. & DeCelles, P.G., 1997. The modern foreland basin system adjacent to the Central Andes, *Geology,* **25,** 895–898.

Husson, L. & Sempere, T., 2003. Thickening the Altiplano crust by gravity-driven crustal channel flow, *Geophys. Res. Lett,* **30,** 1243, doi:10.1029/2002GL016877.

Hyndman, R.D. & Peacock, S.M., 2003. Serpentinization of the forearc mantle, *Earth planet. Sci. Lett.,* **212,** 417–432.

Isacks, B.L., 1988. Uplift of the Central Andean Plateau and bending of the Bolivian Orocline, *J. geophys. Res.-Solid Earth,* **93,** 3211–3231.

Jay, J.A. *et al.*, 2012. Shallow seismicity, triggered seismicity, and ambient noise tomography at the long-dormant Uturuncu Volcano, Bolivia, *Bull. Volcanol,* **74,** 817–837.

Jordan, T.E. & Allmendinger, R.W., 1986. The Sierras Pampeanas of Argentina—a modern analog of rocky-mountain foreland deformation, *Am. J. Sci.,* **286,** 737–764.

Jordan, T.E., Isacks, B.L., Allmendinger, R.W., Brewer, J.A., Ramos, V.A. & Ando, C.J., 1983. Andean tectonics related to geometry of subducted Nazca Plate, *Geol. Soc. Am. Bull.,* **94,** 341–361.

Jordan, T.E., Nester, P.L., Blanco, N., Hoke, G.D., Davila, F. & Tomlinson, A.J., 2010. Uplift of the Altiplano-Puna plateau: a view from the west, *Tectonics,* **29,** TC5007, doi:10.1029/2010TC002661.

Kay, S.M., Coira, B.L., Caffe, P.J. & Chen, C.H., 2010. Regional chemical diversity, crustal and mantle sources and evolution of central Andean Puna plateau ignimbrites, *J. Volc. Geotherm. Res.,* **198,** 81–111.

Kendrick, E., Bevis, M., Smalley, R., Brooks, B., Vargas, R.B., Lauriia, E. & Fortes, L.P.S., 2003. The Nazca South America Euler vector and its rate of change, *J. South Am. Earth Sci.,* **16,** 125–131.

Kley, J., Monaldi, C.R. & Salfity, J.A., 1999. Along-strike segmentation of the Andean foreland: causes and consequences, *Tectonophysics,* **301,** 75–94.

Lamb, S., 2011. Did shortening in thick crust cause rapid Late Cenozoic uplift in the northern Bolivian Andes? *J. geol. Soc. Lond.,* **168,** 1079–1092.

Lamb, S. & Hoke, L., 1997. Origin of the high plateau in the Central Andes, Bolivia, South America, *Tectonics,* **16,** 623–649.

Lange, D. *et al.*, 2012. Aftershock seismicity of the 27 February 2010 Mw 8.8 Maule earthquake rupture zone, *Earth planet. Sci. Lett.,* **317,** 413–425.

Larson, A.M., Snoke, J.A. & James, D.E., 2006. S-wave velocity structure, mantle xenoliths and the upper mantle beneath the Kaapvaal craton, *Geophys. J. Int.,* **167,** 171–186.

Lin, F.C., Moschetti, M.P. & Ritzwoller, M.H., 2008. Surface wave tomography of the western United States from ambient seismic noise: Rayleigh and Love wave phase velocity maps, *Geophys. J. Int.,* **173,** 281–298.

Lin, F.C., Ritzwollerl, M.H., Townend, J., Bannister, S. & Savage, M.K., 2007. Ambient noise Rayleigh wave tomography of New Zealand, *Geophys. J. Int.,* **170,** 649–666.

Lucassen, F. *et al.*, 2001. Composition and density model of the continental crust at an active continental margin—the Central Andes between 21 degrees and 27 degrees S, *Tectonophysics,* **341,** 195–223.

Ma, Y., Clayton, R.W., Tsai, V.C. & Zhan, Z., 2013. Locating a scatterer in the active volcanic area of Southern Peru from ambient noise cross-correlation, *Geophys. J. Int.,* **192**(3), 1332–1341.

Mamani, M., Worner, G. & Sempere, T., 2010. Geochemical variations in igneous rocks of the Central Andean orocline (13 degrees S to 18 degrees S): tracing crustal thickening and magma generation through time and space, *Geol. Soc. Am. Bull.,* **122,** 162–182.

Manning, C.E., 2004. The chemistry of subduction-zone fluids, *Earth planet. Sci. Lett.,* **223,** 1–16.

McQuarrie, N., Barnes, J.B. & Ehlers, T.A., 2008. Geometric, kinematic, and erosional history of the Central Andean Plateau, Bolivia (15–17 degrees S), *Tectonics,* **27,** doi:10.1029/2006TC002054.

Meltzer, A. *et al.*, 1999. USArray initiative, *GSA Today,* **9**, 8–10.

Moschetti, M.P., Ritzwoller, M.H. & Shapiro, N.M., 2007. Surface wave tomography of the western United States from ambient seismic noise: Rayleigh wave group velocity maps, *Geochem. Geophys. Geosyst.,* **8,** Q08010, doi:10.1029/2007GC001655.

Norabuena, E., Leffler-Griffin, L., Mao, A.L., Dixon, T., Stein, S., Sacks, I.S., Ocola, L. & Ellis, M., 1998. Space geodetic observations of Nazca-South America convergence across the central Andes, *Science,* **279,** 358–362.

Oncken, O., Hindle, D., Kley, J., Elger, K., Victor, P. & Schemmann, K., 2006. Deformation of the central Andean upper plate system—facts, fiction, and constraints for plateau models, in *The Andes: Active Subduction Orogeny,* pp. 3–27, eds Oncken, O., Chong, G., Franz, G., Giese, P., Gotze, H.-J., Ramos, V.A., Strecker, M.R. & Wigger, P., Springer-Verlag, Berlin.

Phillips, K. *et al.*, 2012. Structure of the subduction system in southern Peru from seismic array data, *J. geophys. Res.-Solid Earth,* **117,** B11306, doi:10.1029/2012JB009540.

Placzek, C., Quade, J. & Patchett, P.J., 2006. Geochronology and stratigraphy of late Pleistocene lake cycles on the southern Bolivian Altiplano: implications for causes of tropical climate change, *Geol. Soc. Am. Bull.,* **118,** 515–532.

Poli, P., Campillo, M., Pedersen, H. & Grp, L.W., 2012. Body-wave imaging of Earth's mantle discontinuities from ambient seismic noise, *Science,* **338,** 1063–1065.

Porter, R., Gilbert, H., Zandt, G., Beck, S., Warren, L., Calkins, J., Alvarado, P. & Anderson, M., 2012. Shear wave velocities in the Pampean flat-slab region from Rayleigh wave tomography: implications for slab and upper mantle hydration, *J. geophys. Res.-Solid Earth,* **117,** B11301, doi:10.1029/2012JB009350.

Pritchard, M.E. & Simons, M., 2004. An InSAR-based survey of volcanic deformation in the southern Andes, *Geophys. Res. Lett.*, **31,** L15610, doi:10.1029/2004GL020545.

Ramos, V.A. & Folguera, A., 2009. Andean flat-slab subduction through time, *1011 Geol. Soc., Lond., Special Publications,* **327**(1), doi:10.1144/1012SP327.3.

Ramos, V.A., Cristallini, E.O. & Perez, D.J., 2002. The Pampean flat-slab of the Central Andes, *J. South Am. Earth Sci.,* **15,** 59–78.

Richardson, T., Gilbert, H., Anderson, M. & Ridgway, K.D., 2012. Seismicity within the actively deforming Eastern Sierras Pampeanas, Argentina, *Geophys. J. Int.,* **188,** 408–420.

Rousse, S., Gilder, S., Fornari, M. & Sempere, T., 2005. Insight into the Neogene tectonic history of the northern Bolivian Orocline from new paleomagnetic and geochronologic data, *Tectonics,* **24,** TC6007, doi:10.1029/2004TC001760.

Roux, P., Sabra, K.G., Gerstoft, P., Kuperman, W.A. & Fehler, M.C., 2005. P-waves from cross-correlation of seismic noise, *Geophys. Res. Lett.,* **32,** L19303, doi:10.1029/2005GL023803.

Sabra, K.G., Gerstoft, P., Roux, P., Kuperman, W.A. & Fehler, M.C., 2005. Surface wave tomography from microseisms in Southern California, *Geophys. Res. Lett.,* **32,** L14311.

Salisbury, M.J., Jicha, B.R., de Silva, S.L., Singer, B.S., Jimenez, N.C. & Ort, M.H., 2011. Ar-40/Ar-39 chronostratigraphy of Altiplano-Puna volcanic complex ignimbrites reveals the development of a major magmatic province, *Geol. Soc. Am. Bull.,* **123,** 821–840.

Saygin, E. & Kennett, B.L.N., 2010. Ambient seismic noise tomography of Australian continent, *Tectonophysics,* **481,** 116–125.

Schilling, F.R., 2006. Partial melting in the Central Andean crust: a review of geophysical, petrophysical, and petrologic evidence, in *The Andes, Active Subduction Orogeny,* pp. 459–474, eds Oncken, O., Chong, G., Franz, G., Giese, P., Götze, H., Ramos, V., Strecker, M. & Wigger, P., Springer-Verlag, Berlin.

Schilling, F.R. & Partzsch, G.M., 2001. Quantifying partial melt fraction in the crust beneath the Central Andes and the Tibetan plateau, *Phys. Chem. Earth Part A,* **26,** 239–246.

Schmitz, M. *et al.*, 1999. The crustal structure beneath the Central Andean forearc and magmatic arc as derived from seismic studies—the PISCO 94 experiment in northern Chile (21 degrees-23 degrees S), *J. South Am. Earth Sci.,* **12,** 237–260.

Shapiro, N.M., Campillo, M., Stehly, L. & Ritzwoller, M.H., 2005. High-resolution surface-wave tomography from ambient seismic noise, *Science,* **307,** 1615–1618.

Seibert, L. & Simkin, T., 2002. *Volcanoes of the World: an Illustrated Catalog of Holocene Volcanoes and their Eruptions,* Smithsonian Institution, Global Volcanism Program Digital Information Series, GVP-3. Available at: http://www.volcano.si.edu/world/ (last accessed 16 January 2012).

Snoke, J.A. & James, D.E., 1997. Lithospheric structure of the Chaco and Parana Basins of South America from surface-wave inversion, *J. geophys. Res.-Solid Earth,* **102,** 2939–2951.

Sobel, E.R., Hilley, G.E. & Strecker, M.R., 2003. Formation of internally drained contractional basins by aridity-limited bedrock incision, *J. geophys. Res.-Solid Earth,* **108,** 2344, doi:10.1029/2002JB001883.

Sobolev, S.V., Babeyko, A.Y., Koulakov, I., Oncken, O. & Vietor, T., 2006. Mechanism of the Andean orogeny: insight from the numerical modeling, in *The Andes: Active Subduction Orogeny,* pp. 509–531, eds Oncken, O., Chong, G., Franz, G., Giese, P., Gotze, H.-J., Ramos, V.A., Strecker, M.R. & Wigger, P., Springer-Verlag, Berlin.

Sodoudi, F., Yuan, X., Asch, G. & Kind, R., 2011. High-resolution image of the geometry and thickness of the subducting Nazca lithosphere beneath northern Chile, *J. geophys. Res.-Solid Earth,* **116,** B04302, doi:10.1029/2010JB007829.

Strecker, M.R., Alonso, R.N., Bookhagen, B., Carrapa, B., Hilley, G.E., Sobel, E.R. & Trauth, M.H., 2007. Tectonics and climate of the southern central Andes, *Annu. Rev. Earth planet. Sci.,* **35,** 747–787.

Tassara, A., 2005. Interaction between the Nazca and South American plates and formation of the Altiplano-Puna plateau: review of a flexural analysis along the Andean margin (15 degrees-34 degrees S), *Tectonophysics,* **399,** 39–57.

Tassara, A. & Echaurren, A., 2012. Anatomy of the Andean subduction zone: three-dimensional density model upgraded and compared against global-scale models, *Geophys. J. Int.,* **189,** 161–168.

Turienzo, M., Dimieri, L., Frisicale, C., Araujo, V. & Sánchez, N., 2012. Cenozoic structural evolution of the Argentinean Andes at 34°40′S: A close relationship between thick and thin-skinned deformation, *AndGeo,* **39**(2), 317–357.

Victor, P., Oncken, O. & Glodny, J., 2004. Uplift of the western Altiplano plateau: evidence from the Precordillera between 20 degrees and 21 degrees S (northern Chile), *Tectonics,* **23,** TC4004, doi:10.1029/2003TC001519.

von Huene, R. & Ranero, C.R., 2003. Subduction erosion and basal friction along the sediment-starved convergent margin off Antofagasta, Chile, *J. geophys Res.-Solid Earth,* **108,** 2079, doi:10.1029/2001JB001569.

Yang, Y.J., Ritzwoller, M.H., Levshin, A.L. & Shapiro, N.M., 2007. Ambient noise Rayleigh wave tomography across Europe, *Geophys. J. Int.,* **168,** 259–274.

Yang, Y.J., Ritzwoller, M.H., Lin, F.C., Moschetti, M.P. & Shapiro, N.M., 2008. Structure of the crust and uppermost mantle beneath the western United States revealed by ambient noise and earthquake tomography, *J. geophys. Res.-Solid Earth,* **113,** B12310, doi:10.1029/2008JB005833.

Yang, Y.J. *et al.*, 2010. Rayleigh wave phase velocity maps of Tibet and the surrounding regions from ambient seismic noise tomography, *Geochem. Geophys. Geosyst.,* **11,** Q08010, doi:10.1029/2010GC003119.

Yuan, X., Sobolev, S.V. & Kind, R., 2002. Moho topography in the central Andes and its geodynamic implications, *Earth planet. Sci. Lett.,* **199,** 389–402.

Yuan, X. *et al.*, 2000. Subduction and collision processes in the Central Andes constrained by converted seismic phases, *Nature,* **408,** 958–961.

Zandt, G., Leidig, M., Chmielowski, J., Baumont, D. & Yuan, X.H., 2003. Seismic detection and characterization of the Altiplano-Puna Magma Body, central Andes, *Pure appl. Geophys.,* **160,** 789–807.

Zheng, S.H., Sun, X.L., Song, X.D., Yang, Y.J. & Ritzwoller, M.H., 2008. Surface wave tomography of China from ambient seismic noise correlation, *Geochem. Geophys. Geosyst.,* **9,** Q0502, doi:10.1029/2008GC001981.

SUPPORTING INFORMATION

Additional Supporting Information may be found in the online version of this article:

Figure S1. Plot of the casual and acasual segments of the unfiltered cross-correlations calculated from the station LCO (IU) with other stations up to an interstation distance of 500 km.

Figure S2. Plot of the different dispersion travel paths for each of the four periods (10, 20, 30 and 40 s) shown in Fig. 7 with the resolution contour used (thick black line) to crop phase velocity measurements for subsequent use in the shear wave inversion.

Figure S3. Plot of shear wave inversion results from four points selected across our study area where black lines represent our favoured constant velocity starting model (4.6 km s^{-1}) and the results for each of the three other constant velocity starting models (3.1, 3.6 and 4.1 km s^{-1}) are shown as colored lines. The locations of the four selected points are referenced in Fig. 2.

Table S1. Number of interstation dispersion measurements we include and exclude.

Table S2. The minimum and maximum number of days used to calculate the cross-correlations (http://gji.oxfordjournals.org/lookup/suppl/doi:10.1093/gji/ggt166/-/DC1).